Three-Dimensional Elemental Mapping at the Atomic Scale in Bimetallic Nanocrystals

7 AUTHORS, INCLUDING:

Bart Goris
University of Antwerp
34 PUBLICATIONS **656** CITATIONS

SEE PROFILE

Annick De Backer
University of Antwerp
17 PUBLICATIONS **99** CITATIONS

SEE PROFILE

Sandra Van Aert
University of Antwerp
104 PUBLICATIONS **1,550** CITATIONS

SEE PROFILE

Sergio Gómez-Graña
Université Bordeaux 1
10 PUBLICATIONS **408** CITATIONS

SEE PROFILE

Three-Dimensional Elemental Mapping at the Atomic Scale in Bimetallic Nanocrystals

Bart Goris,[†] Annick De Backer,[†] Sandra Van Aert,[†] Sergio Gómez-Graña,[‡] Luis M. Liz-Marzán,[‡,§,‖] Gustaaf Van Tendeloo,[†] and Sara Bals*[,†]

[†]Electron Microscopy for Materials Research (EMAT), University of Antwerp, Groenenborgerlaan 171, 2020 Antwerp, Belgium
[‡]Departamento de Química Física, Universidade de Vigo, 36310 Vigo, Spain
[§]BioNanoPlasmonics Laboratory, CIC biomaGUNE, Paseo de Miramón 182, 20009 Donostia - San Sebastián, Spain
[‖]Ikerbasque, Basque Foundation for Science, 48011 Bilbao, Spain

S *Supporting Information*

ABSTRACT: A thorough understanding of the three-dimensional (3D) atomic structure and composition of core−shell nanostructures is indispensable to obtain a deeper insight on their physical behavior. Such 3D information can be reconstructed from two-dimensional (2D) projection images using electron tomography. Recently, different electron tomography techniques have enabled the 3D characterization of a variety of nanostructures down to the atomic level. However, these methods have all focused on the investigation of nanomaterials containing only one type of chemical element. Here, we combine statistical parameter estimation theory with compressive sensing based tomography to determine the positions and atom type of each atom in heteronanostructures. The approach is applied here to investigate the interface in core−shell Au@Ag nanorods but it is of great interest in the investigation of a broad range of nanostructures.

KEYWORDS: *Electron tomography, atomic scale elemental mapping, bimetallic nanocrystals, statistical parameter estimation*
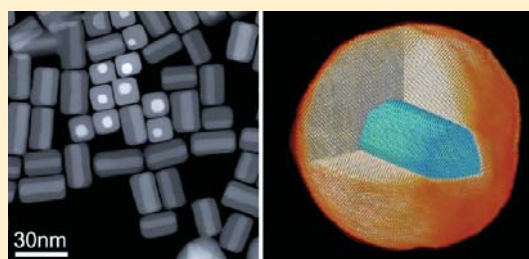
Bimetallic nanostructures are of great interest as they provide additional flexibility, stability, or even novel properties in comparison to their monometallic counterparts.[1−4] As an example, the deposition of Ag-coated Au (Au@Ag) nanorods has been extensively studied because of the possibility to tune their overall geometry (and optical response) by changing the size and aspect ratio of the original Au nanorods.[5−12] Au@Ag nanoparticles cannot only be considered as excellent building blocks for electro-optical devices,[13−15] but they can also be used for applications in surface-enhanced Raman scattering and as contrast agents in biomedical applications.[16−18] However, to understand and tailor these properties a thorough knowledge of the structure and the chemical composition of the nanoparticles at the atomic scale is required. In particular, the atomic structure at the interfaces between the metallic components, including possible effects such as intermixing and alloying, might influence the physical properties of these materials. Ag and Au have almost identical lattice constants (0.408 nm for Au and 0.409 nm for Ag), which may favor alloy formation near the interface, leading for example to shifts of the corresponding plasmon resonance bands.[4,19]

Transmission electron microscopy (TEM) is an ideal tool to investigate both the structure and the chemical composition of multicomponent nanomaterials and interfaces by means of high resolution TEM, energy dispersive X-ray (EDX) mapping, or electron energy loss spectroscopy (EELS).[20,21] Also high-angle annular dark-field (HAADF) scanning transmission electron microscopy (STEM) is a valuable technique to investigate the structure and the composition of nanoparticles. This technique yields projection images in which the intensity scales with the thickness of the sample as well as the atomic number Z.[22,23] As a result, brighter areas in a HAADF-STEM projection of a nanocrystal correspond either to a thicker region or to a region with a higher average atomic number. In this manner, relative chemical information can be obtained from HAADF-STEM projection images.

It is important to realize that all of the techniques described above only yield two-dimensional (2D) projection images of three-dimensional (3D) objects. However, especially for nanostructures it is of crucial importance to characterize their structure and composition in 3D. This can be achieved through electron tomography, a technique in which several 2D projection images can be combined into a 3D reconstruction using a mathematical algorithm. At the nanoscale, such reconstructions yield valuable information on the shape and thickness of the core and shell in bimetallic particles. In order to study the Au−Ag interface in sufficient detail, atomic
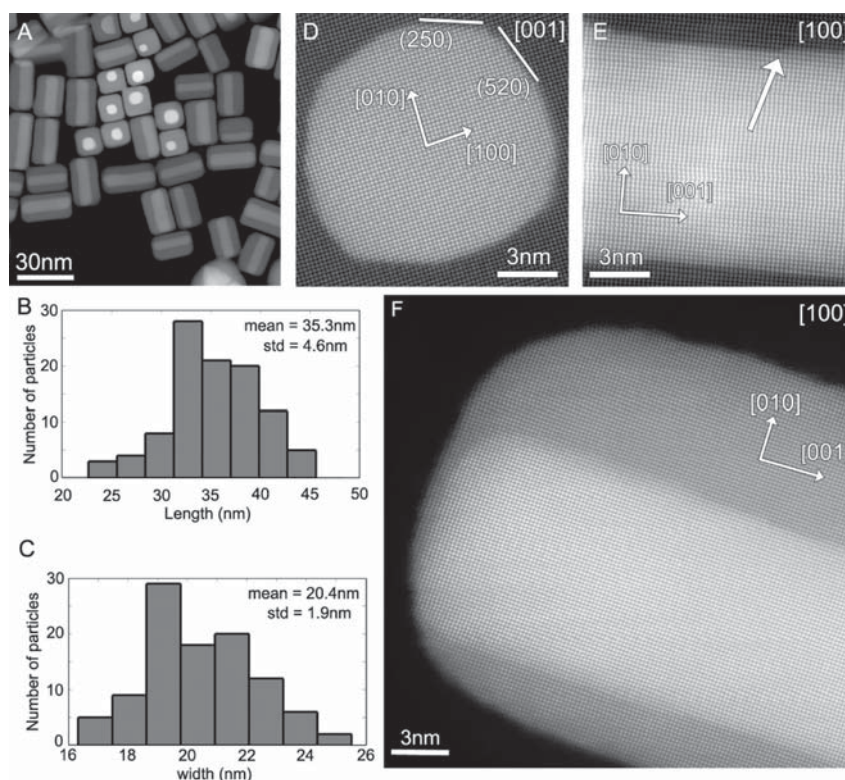
Figure 1. (A) HAADF-STEM projection displaying an overview of the sample. (B,C) Histograms of the length and the width of the nanorods resulting in an average aspect ratio of (1.73 ± 0.28). (D–F) High-resolution HAADF-STEM projection images of a core−shell nanorod along different viewing directions.

resolution electron tomography is required. This technique has recently become available through different approaches.[24−27] Using only four high resolution projection images, we recently applied a 3D reconstruction technique based on compressive sensing[28,29] to reconstruct the atom positions in Au nanorods.[30] In comparison to other approaches,[25,27,31] where a large number of projection images are used as an input, beam damage or structural deformation during acquisition is reduced to a strict minimum when using our method. So far all 3D studies at the atomic scale were dedicated to nanomaterials in which only atoms of one specific chemical element were present. In this paper, we go a step further and determine also the atom type of the individual atoms in an Au@Ag nanorod. In order to distinguish Ag from Au atoms, we combine compressive sensing-based electron tomography with statistical parameter estimation methods. Compressive sensing is a technique that is specialized in finding a solution that is sparse in some basis to a set of underdetermined linear equations. It can therefore be applied to electron tomography at the nanometer scale where the object can either be sparsified in a gradient or in a wavelet basis.[32−36] At the atomic scale, we can use the sparsity of the object itself as explained in previous work.[30]

We investigated Au@Ag core−shell nanorods that were prepared by seeded growth on preformed Au nanorods. A more detailed description of the synthesis method is provided in Materials and Methods. An overview image of the sample, obtained by HAADF-STEM is presented in Figure 1A. Nanorods lying flat on the TEM carbon support as well as nanorods standing perpendicular on the carbon layer can be observed. Because of the chemical sensitivity of HAADF-

STEM, the core and the shell can be clearly distinguished. The average aspect ratio of these nanorods is an important parameter that determines the optical properties of the structures and equals (1.73 ± 0.28). This value was derived from the histograms of the length and width shown in Figure 1B,C, respectively, where it can be seen that the average length is (35.3 ± 4.6) nm whereas the width equals (20.4 ± 1.9) nm. High-resolution HAADF-STEM images of a standing rod (Figure 1D) and a rod lying flat on the carbon layer (Figure 1E,F) demonstrate the face-centered cubic (fcc) atomic lattice and reveal a [100] projection along the major axis (Figure 1D) and perpendicular to the major axis of the nanorod (Figure 1E,F), respectively. In all HAADF-STEM projection images, the interface between Au and Ag appears sharp though steps can sometimes be observed. An example of such a surface step is indicated by the white arrow in Figure 1E.

In order to investigate the general 3D morphology of these nanorods, a conventional HAADF-STEM tilt series (angular range = ±70°; tilt increment = 5°) was acquired. A reconstruction of this series was obtained using the total variation minimization reconstruction technique.[36] The 3D visualizations of the reconstruction are presented in the Supporting Information. From this reconstruction, it is clear that the thickness of the shell is uniform, but in order to investigate the interface in more detail a 3D reconstruction at the atomic scale is required. To reach this goal, five high-resolution HAADF-STEM projection images of the same nanorod were acquired along different major zone axes. These zone axes were chosen along two different tilt axes that are mutually orthogonal in order to minimize artifacts in the final reconstruction.[37] More information on the experimental details

of the acquisition settings can be found in Materials and Methods. The projection images are presented in Figure 2A.
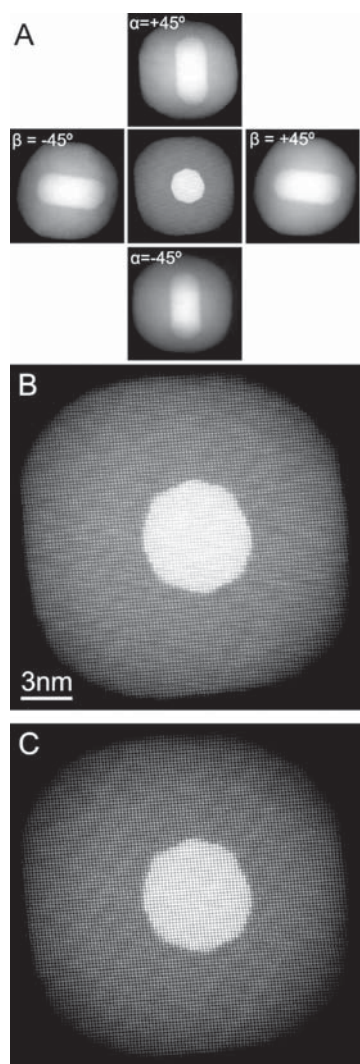

Figure 2. High-resolution HAADF-STEM projection image of an Au/Ag core shell nanorod. (A) Five projection images obtained by tilting the nanorod along the different tilt axes that are mutually orthogonal. (B) More detailed view of the projection at zero degree tilt angle. (C) Refined model of this projection image. Noise and scanning artifacts are reduced in this refined model.

Figure 2B shows the projection image acquired along the major axis of the Au nanorod in more detail. The high-resolution STEM projection image as well as the electron diffraction pattern (presented in the Supporting Information) are consistent with an fcc crystal lattice which is expected for Au and Ag particles of these dimensions. The electron diffraction pattern reveals no splitting, which is in agreement with the negligible mismatch between the lattice parameters of Ag and Au.

In order to obtain a reliable, atomic resolution, 3D reconstruction from these five high-resolution HAADF-STEM projection images, we used an algorithm that is based on compressive sensing. We hereby exploit the sparsity of the nanorod at the atomic scale since it can be expected that only a limited number of voxels contain an atom and that most voxels correspond to vacuum. This methodology was recently used to reconstruct the positions of the atoms in an Au nanorod based on four high-resolution HAADF-STEM projection images.[30] In the present study, our aim was not only to determine the positions of the atoms, but also to identify the atom type of individual atoms. Such identification was based on a quantitative comparison of the intensities of the voxels in the final 3D reconstruction. However, since this process may be strongly influenced by (scanning) noise, we first modeled the projection images in a quantitative manner to reduce such effects. Therefore, a parametric model in which projection images of the atomic columns are described using Gaussian peaks has been assumed. The parameters of this model, including the positions, height, and width of the intensity peaks, were determined using the least-squares estimator.[38−40] An example of a refined model, evaluated at these estimated parameters is shown in Figure 2C. This model is based on the projection image that is displayed in Figure 2B. The other models are presented in the Supporting Information. An excellent agreement between the refined models and the experimental projection images is observed and indeed scanning noise is reduced.

Next, we used the refined models as an input for 3D reconstruction. This resulted in a high resolution reconstruction, which was combined with the reconstruction presented in Figure S1 (Supporting Information), following the approach proposed by Saghi et al.[41] See technical details in the Materials and Methods.

The results of our approach are illustrated in Figure 3, where 3D volume renderings of the reconstruction are shown, a comparison between the reconstruction at low- and high-magnification is presented as Figure S4 in the Supporting Information. In this volume rendering, a visual distinction can be clearly made between the Au core (rendered in yellow) and the surrounding Ag shell (rendered in blue). Figure 3A−C corresponds to visualizations where the sample was tilted by 0, 45, and 90° around the [010] axis, respectively. The resulting Fourier transforms correspond to the expected symmetry for an fcc crystal structure and the atomic lattice can clearly be recognized from the visualizations themselves. An animated view of this reconstruction is supplied as Supporting Information.

A more detailed analysis of the position and type of the atoms was performed by making orthogonal slices through the reconstruction, which are shown in Figure 4. From Figure 4, one can observe minor artifacts in the 3D reconstruction, such as stripes or deformation of the individual atoms. The artifacts observed in Figure 4 are related to (currently) unavoidable sample drift during scanning, remaining scanning noise and the acquisition geometry. Since HAADF-STEM projection images were obtained from the underlying data for the 3D reconstruction, the intensity of each reconstructed atom is related to its atomic weight. Therefore, individual Ag and Au atoms can be distinguished, also at the interface by comparing their relative intensities. An intensity profile was acquired along the direction indicated by the white rectangle in Figure 4B. From this intensity profile, which is presented in Figure 4, it is clear that Au and Ag atoms can indeed be identified from their intensities using a threshold value. In this manner, each atom in the cross sections presented in Figure 4B,C was assigned to be Ag or Au. The result is shown in Figure 4D,E and enabled us to carry out a correct indexing of the type of interfacial planes. We thus conclude that the interface between the Au core and the
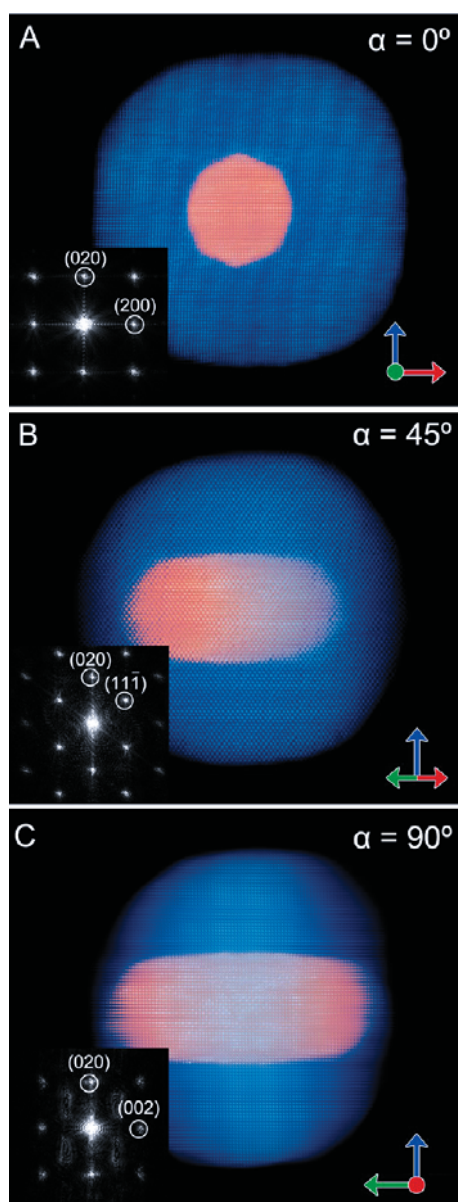
Figure 3. Tomographic reconstruction of an Au@Ag core shell nanorod. (A−C) Volume renderings of the reconstruction viewed along different projection directions where the sample was tilted around the [010] axis for 0, 45, and 90°. In these visualizations, the Au core is rendered yellow whereas the surrounding Ag shell is shown in blue. The Fourier transforms of these projected views correspond to an fcc crystal lattice whereas the atomic structure can be clearly recognized in the visualizations.

Ag shell is sharp, without intermixing and mainly composed of {520} facets where bevels are observed at the ⟨100⟩ and the ⟨110⟩ directions. It should be noted that these {520} facets can be considered as alternating, small {100} and {110} facets. An example of a bevel along a ⟨100⟩ direction is indicated by the arrow in Figure 4D. The presence of these high index facets is in agreement with previous results where the morphology of isolated Au nanorods was observed by 2D and 3D high-resolution TEM.[30,42] At the tips of the Au cores, the interfaces are mainly composed of {001} and {011} facets, as can be seen from the slice through the reconstruction presented in Figure

4E. Furthermore, all surface facets of the core−shell rod are mainly composed of {100} facets while a truncation is observed as small {011} facets, which is also often observed for silver nanocubes.[43] This is furthermore, to the best of our knowledge, the first experiment in which the atom type of individual atoms in a heterostructure is determined in 3D. Atomic resolution chemical maps have previously been reported using EDX or EELS but these results only represent 2D projection images of 3D objects. For samples in which elements with a small difference in atomic number are present, the extension of EELS and EDX from 2D to 3D can be considered as the next challenge. It is currently impossible to investigate effects such as intermixing at the atomic level from 2D projection images. Using the approach presented here, we can conclude that intermixing at the Au−Ag interface is absent and that the major interfacial planes correspond to {520} facets with {001} and {011} facets present at the tips of the Au core. This type of detailed information is of crucial importance to understand and optimize the physical properties of these materials. The absence of intermixing atoms furthermore determines the energy level at which the plasmon modes of the core−shell nanoparticle occur.[4]

In summary, using a combination of statistical parameter estimation and 3D reconstructions, based on compressive sensing, we succeeded to reconstruct the 3D position and type of the atoms in a Au@Ag nanorod. This enables the investigation of the core−shell interface in 3D with atomic sensitivity. It was found that the interface was sharp without intermixing. The type of planes were furthermore found to change from {520} planes at the interface to {100} planes at the outer surface. Our methodology was applied to Au@Ag nanorods but obviously the technique is applicable to a broad range of heteronanostructures. The 3D atomic scale information that can be obtained using the approach we present here will highly contribute to a complete understanding of the growth and properties of nanomaterials.

Materials and Methods. *Sample Preparation.* Au@Ag nanorods were synthesized following a modification of the procedure previously reported by Vaia and co-workers.[8,44] A mixed solution (5 mL) was prepared containing 10 mM benzyldimethylhexadecylammonium chloride (BDAC), 1 mM $AgNO_3$, 4 mM ascorbic acid, and 0.25 mM Au^0 (in the form of previously synthesized gold nanorods). The temperature was then increased up to 60−65 °C and maintained for 3 h. Finally, the obtained solution was centrifuged (6000 rpm 20 min) and redispersed in water.

HAADF-STEM Imaging. HAADF-STEM imaging was performed using the aberration corrected cubed FEI Titan 80−300 electron microscope operated at 300 kV. Tilting to the correct zone axes was achieved by using a motorized tilt rotation tomography holder (Fischione model 2040). The specimen holder was stabilized for 2 min after tilting to minimize sample drift. A probe convergence semi angle of 21.4 mrad was used during the acquisition. To acquire the regular tomography tilt series, a magnification was used corresponding to a pixel size of 0.55 Å. The high-resolution STEM projection images yield a pixel size of 0.14 Å. A camera length of 115 mm was used to ensure the incoherent image formation process corresponding to inner and outer collection angles of 41 and 95 mrad, respectively.

Statistical Parameter Estimation. In order to obtain a high-quality 3D reconstruction, reduction of the effect of scanning noise is important. Therefore, we employed statistical
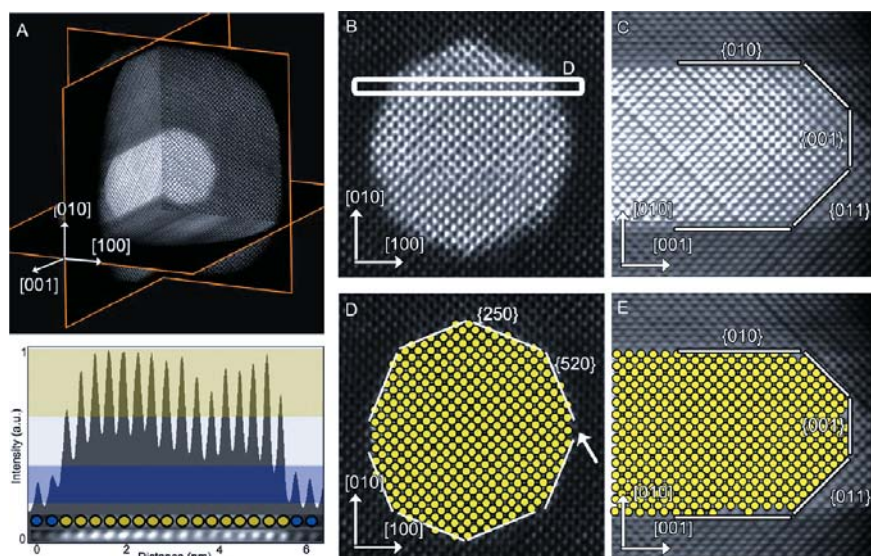
Figure 4. Orthogonal slices through the 3D reconstruction. (A) Three orthogonal slices through the reconstruction show the core−shell structure of the nanorod. The atomic lattice can be resolved in all three slices. (B,C) Detailed view of slices through the reconstruction perpendicular and parallel to the major axis of the nanorod. An intensity profile is acquired along the direction indicated by the white rectangle in (B). (D,E) Slices corresponding to B and C, in which each Au atom is indicated by a yellow circle. In this manner, the correct interfacial planes can be determined based on intensity profiles through the reconstruction.

parameter estimation methods to the 2D projection images. When using this methodology, a parametric model in which projections of atoms are described using Gaussian peaks was assumed. This model accurately describes the imaging contrast of the high-resolution HAADF-STEM projection images. The parameters of this model, including the positions, height, and width of the intensity peaks, were estimated by minimizing the least-squares sum. This criterion describes the correspondence between the projection images and the model. However, to avoid that this criterion of goodness of fit would converge to a local rather than a global minimum, appropriate starting values for the parameters are required. Such values were provided by means of template matching.

Reconstruction Method. Prior to using the statistical models for the reconstruction, a constant background value is subtracted from the projection images to ensure that a zero intensity value in the projection images is invoked by a projection ray that has not passed any atoms. These projection images are then aligned using a combination of a manual alignment performed in IMOD[45] and using the center of mass as a reference point as proposed in previous studies.[25,30] The high-resolution reconstruction is obtained by minimizing the L1 norm of the reconstructed object (i.e., the sum of the absolute values) together with the projection distance (i.e., the difference between the original projection images and the simulated ones from an intermediate reconstruction) as explained in ref 30. During this minimization, a penalty parameter is used that equals 0.5. This penalty parameter is optimized based on previous (simulation) experiments and indicates the importance of the L1-minimization. It must be noted that during the reconstruction no assumptions are made concerning the periodicity or the crystal lattice of the nanorod. Afterward, the result is improved using a mask that is created using a tomography reconstruction obtained from more projection images as proposed by Saghi et al.[41] This mask reduces the presence of artifacts that appear during the reconstruction due to the limited number of projection images.

■ ASSOCIATED CONTENT

Ⓢ Supporting Information

Tomography at regular magnification, refined models of all projection images, electron diffraction of Au@Ag nanorods, and comparison between low- and high-magnification reconstruction. This material is available free of charge via the Internet at http://pubs.acs.org.

■ AUTHOR INFORMATION

Corresponding Author
*E-mail: sara.bals@ua.ac.be.
Notes
The authors declare no competing financial interest.

■ ACKNOWLEDGMENTS

■ REFERENCES

(1) Henglein, A. *J. Phys. Chem. B* **2000**, *104* (10), 2201−2203.
(2) Hodak, J. H.; Henglein, A.; Hartland, G. V. *J. Phys. Chem. B* **2000**, *104* (21), 5053−5055.
(3) Tedsree, K.; Li, T.; Jones, S.; Chan, C. W. A.; Yu, K. M. K.; Bagot, P. A. J.; Marquis, E. A.; Smith, G. D. W.; Tsang, S. C. E. *Nat. Nanotechnol.* **2011**, *6* (5), 302−307.
(4) Cortie, M. B.; McDonagh, A. M. *Chem. Rev.* **2011**, *111* (6), 3713−3735.

(5) Liu, M. Z.; Guyot-Sionnest, P. *J. Phys. Chem. B* **2004**, *108* (19), 5882−5888.

(6) Yang, Z. S.; Chang, H. T. *Nanotechnology* **2006**, *17* (9), 2304−2310.

(7) Xiang, Y. U.; Wu, X. C.; Liu, D. F.; Li, Z. Y.; Chu, W. G.; Feng, L. L.; Zhang, K.; Zhou, W. Y.; Xie, S. S. *Langmuir* **2008**, *24* (7), 3465−3470.

(8) Park, K.; Drummy, L. F.; Vaia, R. A. *J. Mater. Chem.* **2011**, *21* (39), 15608−15618.

(9) Ma, Y. Y.; Li, W. Y.; Cho, E. C.; Li, Z. Y.; Yu, T. K.; Zeng, J.; Xie, Z. X.; Xia, Y. N. *ACS Nano* **2010**, *4* (11), 6725−6734.

(10) Cho, E. C.; Camargo, P. H. C.; Xia, Y. N. *Adv. Mater.* **2010**, *22* (6), 744.

(11) Sanchez-Iglesias, A.; Carbo-Argibay, E.; Glaria, A.; Rodriguez-Gonzalez, B.; Perez-Juste, J.; Pastoriza-Santos, I.; Liz-Marzan, L. M. *Chem.—Eur. J.* **2010**, *16* (19), 5558−5563.

(12) Cardinal, M. F.; Rodriguez-Gonzalez, B.; Alvarez-Puebla, R. A.; Perez-Juste, J.; Liz-Marzan, L. M. *J. Phys. Chem. C* **2010**, *114* (23), 10417−10423.

(13) Becker, J.; Zins, I.; Jakab, A.; Khalavka, Y.; Schubert, O.; Sonnichsen, C. *Nano Lett.* **2008**, *8* (6), 1719−1723.

(14) Li, M.; Zhang, Z. S.; Zhang, X.; Li, K. Y.; Yu, X. F. *Opt. Express* **2008**, *16* (18), 14288−14293.

(15) Wang, L.; Kiya, A.; Okuno, Y.; Niidome, Y.; Tamai, N. *J. Chem. Phys.* **2011**, *134*, 054501.

(16) Chen, J. Y.; Wiley, B.; Li, Z. Y.; Campbell, D.; Saeki, F.; Cang, H.; Au, L.; Lee, J.; Li, X. D.; Xia, Y. N. *Adv. Mater.* **2005**, *17* (18), 2255−2261.

(17) Hunyadi, S. E.; Murphy, C. J. *J. Mater. Chem.* **2006**, *16* (40), 3929−3935.

(18) Gómez-Graña, S. P.-J., J.; Alvarez-Puebla, R. A.; Guerrero-Martínez, A.; Liz-Marzán, L. M. *Adv. Opt. Mater.* **2013**.

(19) Zhu, J.; Wang, Y. C.; Lu, Y. M. *Colloid Surf., A* **2004**, *232* (2−3), 155−161.

(20) Krivanek, O. L.; Chisholm, M. F.; Nicolosi, V.; Pennycook, T. J.; Corbin, G. J.; Dellby, N.; Murfitt, M. F.; Own, C. S.; Szilagyi, Z. S.; Oxley, M. P.; Pantelides, S. T.; Pennycook, S. J. *Nature* **2010**, *464* (7288), 571−574.

(21) Van Tendeloo, G.; Bals, S.; Van Aert, S.; Verbeeck, J.; Van Dyck, D. *Adv. Mater.* **2012**, *24* (42), 5655−5675.

(22) Hartel, P.; Rose, H.; Dinges, C. *Ultramicroscopy* **1996**, *63* (2), 93−114.

(23) Nellist, P. D.; Pennycook, S. J. *Adv. Imaging Electron Phys.* **2000**, *113*, 147−203.

(24) Bals, S.; Casavola, M.; van Huis, M. A.; Van Aert, S.; Batenburg, K. J.; Van Tendeloo, G.; Vanmaekelbergh, D. *Nano Lett.* **2011**, *11* (8), 3420−3424.

(25) Scott, M. C.; Chen, C. C.; Mecklenburg, M.; Zhu, C.; Xu, R.; Ercius, P.; Dahmen, U.; Regan, B. C.; Miao, J. W. *Nature* **2012**, *483* (7390), 444−U91.

(26) Van Aert, S.; Batenburg, K. J.; Rossell, M. D.; Erni, R.; Van Tendeloo, G. *Nature* **2011**, *470* (7334), 374−377.

(27) Chen, C. C.; Zhu, C.; White, E. R.; Chiu, C. Y.; Scott, M. C.; Regan, B. C.; Marks, L. D.; Huang, Y.; Miao, J. W. *Nature* **2013**, *496* (7443), 74−+.

(28) Donoho, D. L. *IEEE Trans. Inf. Theory* **2006**, *52* (4), 1289−1306.

(29) Baraniuk, R. G.; Candes, E.; Elad, M.; Ma, Y. *P Ieee* **2010**, *98* (6), 906−909.

(30) Goris, B.; Bals, S.; Van den Broek, W.; Carbo-Argibay, E.; Gomez-Grana, S.; Liz-Marzan, L. M.; Van Tendeloo, G. *Nat. Mater.* **2012**, *11* (11), 930−935.

(31) Bar Sadan, M.; Houben, L.; Wolf, S. G.; Enyashin, A.; Seifert, G.; Tenne, R.; Urban, K. *Nano Lett.* **2008**, *8* (3), 891−896.

(32) Song, K.; Comolli, L. R.; Horowitz, M. *J. Struct. Biol.* **2012**, *178* (2), 108−120.

(33) Saghi, Z.; Holland, D. J.; Leary, R.; Falqui, A.; Bertoni, G.; Sederman, A. J.; Gladden, L. F.; Midgley, P. A. *Nano Lett.* **2011**, *11* (11), 4666−4673.

(34) Monsegue, N.; Jin, X.; Echigo, T.; Wang, G.; Murayama, M. *Microsc. Microanal.* **2012**, *18* (6), 1362−1367.

(35) Leary, R.; Saghi, Z.; Midgley, P. A.; Holland, D. J. *Ultramicroscopy* **2013**, *131C*, 70−91.

(36) Goris, B.; Van den Broek, W.; Batenburg, K. J.; Mezerji, H. H.; Bals, S. *Ultramicroscopy* **2012**, *113*, 120−130.

(37) Arslan, I.; Tong, J. R.; Midgley, P. A. *Ultramicroscopy* **2006**, *106* (11−12), 994−1000.

(38) den Dekker, A. J.; Van Aert, S.; van den Bos, A.; Van Dyck, D. *Ultramicroscopy* **2005**, *104* (2), 83−106.

(39) Van Aert, S.; den Dekker, A. J.; van den Bos, A.; Van Dyck, D.; Chen, J. H. *Ultramicroscopy* **2005**, *104* (2), 107−125.

(40) Van Aert, S.; Verbeeck, J.; Erni, R.; Bals, S.; Luysberg, M.; Van Dyck, D.; Van Tendeloo, G. *Ultramicroscopy* **2009**, *109* (10), 1236−1244.

(41) Saghi, Z.; Xu, X. J.; Mobus, G. *J. Appl. Phys.* **2009**, *106*, 2.

(42) Carbo-Argibay, E.; Rodriguez-Gonzalez, B.; Gomez-Grana, S.; Guerrero-Martinez, A.; Pastoriza-Santos, I.; Perez-Juste, J.; Liz-Marzan, L. M. *Angew. Chem., Int. Ed.* **2010**, *49* (49), 9397−9400.

(43) Wiley, B.; Herricks, T.; Sun, Y. G.; Xia, Y. N. *Nano Lett.* **2004**, *4* (9), 1733−1739.

(44) Gomez-Graña, S.; Goris, B.; Altantzis, T.; Fernández-López, C.; Carbó-Argibay, E.; Guerrero-Martínez, A.; Almora-Barrios, N.; López, N.; Pastoriza-Santos, I.; Pérez-Juste, J.; Bals, S.; Van Tendeloo, G.; Liz-Marzán, L. M. *J. Phys. Chem. Lett.* **2013**, *4*, 2209−2216.

(45) Kremer, J. R.; Mastronarde, D. N.; McIntosh, J. R. *J. Struct. Biol.* **1996**, *116* (1), 71−76.